Magnetic quantification of single crystal Fe and Co nanowires via off-axis electron holography

Ke Chai[a,b], Zi-An Li[b]*, Wenting Huang[c,d], Gunther Richter[d], Ruibin Liu[a]*, Bingsuo Zou[a], András Kovács[e], Rafal E. Dunin-Borkowski[e], and Jianqi Li[b]

[a] Beijing Key Laboratory of Nano photonics and Ultrafine Optoelectronic Systems, School of Physics, Beijing Institute of Technology，Beijing 100081, P. R. China

[b] Beijing National Laboratory for Condensed Matter Physics and Institute of Physics, Chinese Academy of Sciences, Beijing 100190, P. R. China

[c] Institute for Applied Materials, Karlsruhe Institute of Technology, Hermann-von-Helmholtz-Platz 1, D-76344 Eggenstein-Leopoldshafen, Germany.

[d] Max Planck Institute for Intelligent Systems, Heisenbergstrasse 3, D-70569 Stuttgart, Germany.

[e] Ernst Ruska-Centre for Microscopy and Spectroscopy with Electrons and Peter Grünberg Institute, Forschungszentrum Jülich, D-52425 Jülich, Germany.

*Corresponding authors

E-mail: zali79@iphy.ac.cn (Zi-An Li) and liusir@bit.edu.cn (Ruibin Liu)

hat formatiert: Englisch (USA)

Abstract

We report on the synthesis of high-quality single crystal Fe and Co nanowires (NWs) via physical vapor deposition (PVD) method, and the magnetic quantification of these NWs at the single wire level using off-axis electron holography (EH) in the transmission electron microscope (TEM). Electron diffraction, lattice imaging, and energy-filtered imaging are employed to examine the single crystalline nature of these NWs. The Fe NWs are found to have a body-centered-cubic structure (α-Fe) with a preferential growth direction of [100], and the Co NWs are face-centered-cubic structure (β-Co) with a preferential growth direction of [220]. EH measurements with *in situ* magnetizing process in the TEM are performed to obtain magnetic induction field distributions of single Fe and Co NWs. These magnetic NWs are found to be uniformly magnetized along the preferential growth direction (axial direction) of the wire, and their average magnetizations are measured to be very close to the values of the respective bulk materials. Our results provide a useful synthesis approach for the growth of single crystalline, defect-free magnetic NWs, and also exemplify a unique EH tool to study nanomagnetic materials on a single nanostructure level.

KEYWORDS Ferromagnetic Nanowires, Micromagnetic Structure, Off-axis Electron Holography, Transmission Electron Microscope

1. Introduction

Owing to their novel magnetic properties that arise from the unique quasi-one-dimensional (1D) structure, there have been intense research interests in magnetic nanowires (NWs) from both academic and applied perspectives for the last few decades[1-4]. Envisioned applications in different fields range from basic units for miniaturized magnetic sensors to magnetic elements for building racetrack-type data storage and magnetic logical devices[5, 6]. To realize these applications, the very first step is to fabricate high-quality magnetic nanowire structures. In this regard, several fabrication routes, including wet-chemistry[7], electrochemical deposition (ECD) with porous alumina templates[8, 9], chemical and physical vapor depositions (CVD[10-12] and PVD), and focused electron-beam-induced deposition (FEBID)[13, 14], have been established to obtain various types of 1D magnetic structures. Generally, most of the magnetic NWs fabricated via ECD and FEBID techniques are found to be polycrystalline with various grain sizes and possess a high density of crystalline grain boundary defects. Wet-chemistry method can effectively synthesize single crystalline compound and oxide-type magnetic NWs, but the synthesis of single crystalline single-element (Fe, Co, Ni) magnetic NWs is still a challenge. Using PVD approach, we have previously demonstrated the growth of free-standing single crystalline nano whiskers of a variety of different materials (copper, gold, silver, aluminum, and silicon) on partially carbon-coated, oxidized Si (100), (110), and (111) substrates under molecular beam epitaxy (MBE) conditions[15]. In this study, we further explore the PVD scheme to synthesize single-crystalline, single-element Fe and Co magnetic NWs.

The structural and magnetic properties of as-synthesized NWs can be examined via a range of micro-spectroscopy and magnetometry characterization tools[16]. Conventional x-ray diffraction and magnetometry (e.g., SQUIDs) measurements were usually carried out on a large assemble of NWs[17-19], and yielded only averaged structural and magnetic information because of their relatively poor spatial resolution and limited sensitivity for nanosized samples. By contrast, TEM techniques can provide a structural and compositional characterization of materials with atomic scale resolution[20]. Moreover, imaging of magnetic domain walls is routinely performed on magnetic thin films by using Lorentz microscopy[21]. Lorentz Fresnel imaging has difficulties in observing magnetic contrasts in sub-100nm-diameter NW structures due to the dominant Fresnel fringe contrasts at the boundaries of the NWs. EH in the TEM, on the other hand, can allow for the recording of phase shifts of high-energy electron waves that pass through samples with a nanometric spatial resolution[22-24]. The recorded phase shifts directly reflect the magnetic and electrostatic potentials in and around the specimen. Some representative EH studies of magnetic nanostructures include the EH studies of various types of magnetic nanostructures reviewed by Rafal E. Dunin-Borkowski et al.[25], the quantitative determination of nanoscale spin textures in 20-nm iron nanocubes by Snock et al.[26], and the three-dimensional magnetic induction field distribution of Co NWs by Wolf and coworkers[27]. TEM-based EH technique is now considered an ideal tool for studying the magnetic properties of materials at single nanostructure level[1, 28].

In this study, we first employed the PVD method to explore the synthesis of single

crystalline Fe and Co magnetic NWs. We then used electron diffraction, high-resolution TEM and energy-filtered imaging to characterize the structural and compositional properties of these as-synthesized NWs with atomic scale resolution. Additionally, we used the EH technique to obtain magnetic induction fields of these NWs on a single nanowire level. These Fe and Co NWs with high-aspect-ratio (tens of micrometers in length and tens of nanometers in diameter) were found to be single crystalline without planar defects and exhibit a magnetic single domain state.

2. Experimental Section

Sample preparation.

The synthesis of Fe and Co NWs were carried out in an Ultra High Vacuum (base pressure ~10^{-10} mbar) - Molecule Beam Epitaxial system (DCA Instruments, Finland). Ultra-pure Fe and Co were placed in crucibles located in effusion cells, heated via a filament. In order to activate the atom diffusion on the substrate surface, which was crucial for the nucleation and subsequent growth of the crystal whiskers, the substrate was heated to nearly 60% of the melting temperature (T_{Fe} = 800°C, T_{Co} = 760°C). In our case, the Fe and Co whiskers were grown directly on Mo wires (0.45 mm diameter) without any pretreatment.

Composition and structure properties measurements.

The bright-field TEM and the corresponding selected-area electron diffraction (SAED) were performed on a TEM (JEM-ARM 200F) with spherical aberration correctors integrated into the image-forming system and the illumination system.

The elemental mappings of whiskers were measured on energy dispersive X-ray (EDS) detector in the same microscope.

Electron holography characterization.

Off-axis electron holograms were acquired in the Lorentz mode using an image-aberration-corrected microscope (FEI Titan 60-300) that is dedicated to EH and *in situ* TEM measurements. This microscope operates with an ultrahigh-brightness field emission gun and was equipped with a wide pole piece gap. The gold coated thin electrostatic biprism (<1-μm) was located at the position of the selection area aperture and was electrostatically biased by hundreds of volts. Applying a suitable positive voltage (~100V) to the biprism causes overlap between the objective wave and reference wave, and results in the formation of the interference fringe pattern on the detector (holographic interference fringe spacing is about 2.8 nm).

In order to extract magnetic field distributions from the recorded phase shift, we used an *in situ* magnetizing process. To mitigate the phase artifacts introduced by electromagnetic lens distortions and biprism charging effects, we also recorded a reference hologram without the specimen under otherwise identical illumination conditions. To reduce the noises in the phase images, a cumulative acquisition approach was used to record 30 holograms with an exposure time of 2s for each hologram. A set of custom-made Matlab codes was used to reconstruct phase images via Fourier transform and band filter method, and to align multiple phase image via cross-correlation method prior to averaging the phase images for enhanced phase sensitivity. To separate electric and magnetic phase contributions, pairs of phase images

of reversed magnetization distributions were manually aligned and subtracted one by another.

3. Results and Discussion

The morphology and crystal structure of the as-synthesized NWs were first examined by scanning electron microscopy (SEM) and TEM, respectively. Fig. 1a shows an SEM image of Fe NWs sparsely grown on the Mo substrate. The Fe wires exhibit variations in diameter (tens to hundreds of nm) and in length (a few to tens of μm), and upon close examination most of them have a tapered whisker-like morphology with a sharp apex. For TEM observations, Fe NWs have been scratched off Mo substrates and transferred to Cu-grids. Fig. 1b shows a representative bright-field TEM image of a Fe nanowire together with one of the corresponding SAED patterns as an inset. Several SAED patterns with sharp spots taken along the nanowire axis reveal the single crystal nature of the nanowire without planar-type twinning or stacking fault defects. The SAED patterns can be indexed with a body-centered cubic (BCC) structure (α-Fe), and the preferential growth direction (length axis) can be determined to be along the <100> crystallographic direction.

Similar SEM and TEM measurements on the Co NWs were also carried out. Fig. 1c shows the typical morphology of Co NWs sparsely grown on Mo substrate. Note that in comparison to the growth of Fe NWs, the density of Co NWs is much less and the lengths of Co are apparently longer than that of Fe NWs. Fig. 1d shows the TEM image of Co NWs and one of its corresponding SAED patterns, revealing the single crystal

nature with no twinning defects or planar stacking faults, similar to the results of Fe NWs. The SAED patterns can be indexed with a Co face-centered cubic (FCC) structure, and also reveal the preferential growth direction of Co NWs to be along the <220> crystallographic direction.

It is well known that Fe and Co are prone to oxidize rapidly upon exposure to ambient conditions, which makes them inappropriate for many applications. In the present study, although the Fe and Co NWs were produced in an ultra-high vacuum molecular beam epitaxy chamber with a base pressure of below $2x10^{-10}$ mbar, the as-obtained NWs were exposed to ambient conditions, and transferred to TEM grids for TEM observation. It is expected that surface layers of Fe and Co NWs can be oxidized under ambient conditions. To examine the extent of oxidation of these NWs, we perform elemental mapping of energy-dispersive x-ray (EDX) characteristic spectroscopy on the Fe NWs in a STEM mode. Figure 2a shows a High-Angle Annular Dark Field (HADDF) image of Fe tip apex. Figure 2b shows the EDX map of iron in the nanowire, and Fig. 2c is the oxygen map in the nanowire, from which one can see the thick shell of oxide around the nanowire.

We then carried out high resolution lattice imaging on the Fe and Co NWs. Fig.2d shows the [001]-oriented Fe nanowire with a distinct contrast of oxide shell, which is also reflected in the fast Fourier transform (FFT) patterns of the shell and core regions (insets to Fig. 2d). In the oxide shell region, a typical lattice spacing of ~ 0.83 nm is measured, which can be associated with the iron oxide phase of either Fe_3O_4 or γ-Fe_2O_3. Similar HRTEM analysis of Co nanowires were carried out, and Fig. 2e shows the

lattice image of a [100]-oriented Co nanowire. The oxide shell develops an epitaxial relation with the whisker core, which is evident from the presence of the moiré fringes. Two sets of spots were observed on the FFT pattern: ones from the Co core (red circle) and the others from the oxide shell (yellow circle). Analysis of the FFT pattern reveals an epitaxial relationship between the oxide and the FCC Co core as $(001)_{oxide}||(001)_{Co}$ and $[100]_{oxide}||[100]_{Co}$. Note that some spots are due to the presence of the moiré (blue circle).

Taking together the high-resolution lattice image, diffraction pattern and the EDX map, the iron nanowires with a thin oxide shell of 5 nm were obtained. It is noted that the nanowires were examined after nearly two years of storage, the thin oxide shell do not further develop, which is due to the passivation oxide shell in iron nanowire against complete oxidation at ambient conditions.

In order to investigate the magnetic properties of the synthesized magnetic NWs at single nanowire level, we used the off-axis EH technique to image magnetic field distributions of NWs with nanometers resolution. The EH technique has been established as an indispensable tool for studies of magnetic properties of nanostructures[29]. Fig 3a shows a schematic representation of the EH setup in the TEM, in which the electron interference pattern (i.e., hologram) can be recorded by overlapping two coherent electron waves by the action of electrostatically charged biprism. The total phase shift recorded using off-axis EH is sensitive to both the electrostatic potential and the in-plane magnetic induction field in the specimen. To extract the magnetic contribution to the phase shift, the directions of magnetization in

NWs were reversed *in situ* in the TEM by tilting the sample ±75º and turning on the conventional microscope objective lens to apply a magnetic field of about 1.5 T to the sample in the electron beam direction. The objective lens was then turned off and the sample tilted back to zero-degree for hologram acquisition in a near field-free condition (residual field of 0.5 mT) with the specimen at remanence. After *in situ* magnetizing process, holograms were recorded with the specimen reversely magnetized so that the mean inner potential (MIP) contributions can be separated from the magnetic potential ones, as described previously[30]. The reconstructed phase images are shown in Fig. 3d and 3e. The difference in the magnetic phase images indicates the reversal of magnetization in the nanowire (NW) due to the *in situ* magnetizing process. The electric phase image equals to the half of the summation of the two phases (Fig. 3f), and the magnetic phase image equals to the half of the subtraction between the two phases (Fig. 3g), provided the magnetization distribution in the two remanent states are completely reversed.

To study the static magnetic structure of individual Fe NW at remanence, a well-isolated single NW with its apex part suspending on the Cu-grid was selected, as shown in Fig. 4a. The NW was partly (~3 um in length), suspended on the edge of TEM grid making the apex part of the NW ideal specimen for off-axis EH measurements. Note that by tilting the NWs and judging from the foreshortened image of tilted NWs, we confirm that the end parts of long NWs are lying flat on the Cu-grid. The electric and magnetic phase images of the apex part of the NW are shown in Fig. 3f and 3g. From the electric phase, one can estimate the thickness variation in the specimen by assuming

a single value of electrostatic mean inner potential (MIP) for the specimen. With the uniform MIP assumption of 21 V for Fe[31], we obtain a rectangular cross-section from the measured electric phase map of Fe NW, and the average thickness is about 55 nm by using phase formula $\Phi_E = C_E \cdot V_0 \cdot t$, where t is the specimen thickness, C_E is the electron microscope constant and takes the values of $6.53*10^6$ $\mathrm{rad}/V \cdot m$[29].

Fig. 4b shows the magnetic phase map of the apex part of the Fe NW. In order to visualize the magnetic induction fields inside and around the magnetic Fe NW, we construct the equal-phase map by computing the cosine-function of the magnetic phase map (6x amplified prior to applying cosine) as shown in Fig. 4c. From the cosine-phase-map, the stray fields emanating from the tip of the Fe NW are clearly seen, while inside the NW, the equal-phase lines are too dense to be seen due to the stronger induction fields inside the NW. Note that specific phase contrasts[2] that can be associated with the formation of domain walls in the NW were not observed, suggesting that at remanence the NW exhibits a uniformly magnetized state with its magnetization direction pointing along the NW length axis. The uniformly magnetized state in NW allows one to estimate the magnetic induction by using the following formula[32]:

$$B = \frac{\hbar \Delta\phi}{eS},$$

where B is magnetic flux density of NW, $\hbar$ is the reduced Plank's constant, e is electron charge, $\Delta\phi$ is phase difference across the NW diameter, and S is cross-section of the NW, provided that the stray fields outside the NW is negligibly weak or not contributing to the phase difference $\Delta\phi$. However, due to the strong strayed fields around the tip apex of the wire, one should avoid using the phase difference near the tip apex. Instead,

magnetic phase differences at the NW positions further away from the tip can be used to measure the induction B. Fig. 4c plots the line profiles of magnetic phase across the NW, in which the red, blue and green phase profiles measured at 600 nm, 400 nm and 200 nm distance away from the NW apex, respectively, as marked in the phase map in Fig. 4b. One can see the line profile of phase difference at 600 nm distance from the tip of NW is far enough to be used for measuring magnetic induction B. From this phase profile, the magnetic flux density $B_{\perp}$ is measured to be 2.07(±0.10) T, which is in good agreement with the value of bulk Fe (2.15 T). Note that the magnetic easy-axis of α-Fe is [100][33] and the long axis of Fe NWs is also along the [100]-axis, making the Fe NWs stay in a single domain state at remanence after in situ magnetizing process in the microscope. The 10% relative high measurement errors are taken from the phase sensitivity only, and it may become larger when considering other sources of error, particularly, the oxide surface layers on Fe nanowires could lead to measurement errors of NW thickness.

Similar EH experiments were carried out on the Co NWs. One suitable Co NWs for EH measurement was shown in Fig. 5a, whose length is more than 12 μm and diameter is about 70 nm. Electrostatic potential phase images and magnetic phase images were obtained by the above mentioned *in situ* magnetizing process and phase separation method. Fig. 5b shows the magnetic phase image of the apex part of the Co NWs, in which two lines mark the positions (200 nm and 500 nm away from the apex) for magnetic phase profiles. To illustrate the projected magnetic induction field distributions, an equal-phase map was constructed (Fig. 5c) in the form of cosine-

function, from which the white-black contrast maps represent the projected induction field lines. Similar to the case of Fe NW in Fig. 4c, the emanating stray field lines outside the apex and field lines inside the part of NW suggest that the Co NW is uniformly magnetized along the NW axis. Thus, one can apply a simple relationship between the phase shifts (magnetic phase profiles across the wire diameter) and the magnetic flux to estimate the mean magnetic induction of the NW. Fig. 5d shows the extracted magnetic phase shifts that can be used to calculate the magnetic flux density of Co NW, provided the cross-section of Co NW is known. The measured value is 1.83(±0.15) T for this Co NW, which is in close agreement with the value of 1.81 T for Co bulk[33]. Due to the Co NW with high aspect ratio (tens of micron in length versus tens of nanometer in diameter), the shape anisotropy of Co NW dominates the magnetocrystalline anisotropy of β-Co with its easy-axis along [111] direction[33]. Consequently, the Co NW is magnetization along the long-axis with [110] crystallographic direction.

4. Conclusion

In summary, we have successfully synthesized single crystal Fe and Co NWs via physical vapor deposition method. We used a range of TEM techniques to study the crystallinity and composition of the as-synthesized NWs. Electron diffraction and high-resolution lattice imaging reveal the single crystalline nature of these NWs. The surface of the Fe and Co NWs were covered by thin (~5 nm) passivation layers of oxides that prevent their further oxidation under ambient conditions, as revealed by energy-filtered

imaging. To quantify the magnetic properties of Fe and Co NWs, we perform *in situ* magnetizing process and EH measurement to obtain the magnetic induction field distributions of single Fe and Co NWs. Analyses of the EH experiment reveal that these Fe and Co magnetic NWs were uniformly magnetized along the length-axis of the wire, and their averaged magnetic induction field strengths are measured to be 2.07(±0.10) T for Fe and 1.83(±0.15) T for Co, which are very close to the values of the respective bulks. Our results demonstrate a route to synthesize high quality, single crystal Fe and Co magnetic NWs and exemplify magnetic quantification of nanomaterials at the single nanostructure level.

Acknowledgements

This work was supported by the National Key Research and Development Program of China (No. 2017YFA0303000), the National Natural Science Foundation of China (No. 11447703, 61574017), and the Graduate Technological Innovation Project of Beijing Institute of Technology (No. 2018CX20029). Z.-A. L acknowledges the Hundred Talent Program B of Chinese Academy of Sciences.

References

1. G.L. Drisko, C. Gatel, P.-F. Fazzini, A. Ibarra, S. Mourdikoudis, V. Bley, K. Fajerwerg, P. Fau, M. Kahn, *Nano Lett.*, 2018, **18**, 1733-1738.
2. N. Biziere, C. Gatel, R. Lassalle-Balier, M.C. Clochard, J.E. Wegrowe, E. Snoeck, *Nano Lett.*, 2013, **13**, 2053.
3. K. Soulantica, F. Wetz, J. Maynadié, A. Falqui, R.P. Tan, T. Blon, B. Chaudret, M. Respaud, *Appl. Phys. Lett.*, 2009, **95**, 152504.
4. G. Dumpich, T.P. Krome, B. Hausmanns, *J. Magn. Magn. Mater.*, 2002, **248**, 241-247.
5. D.A. Allwood, G. Xiong, C.C. Faulkner, D. Atkinson, D. Petit, R.P. Cowburn, *Science*, 2005, **309**, 1688.
6. S.S.P. Parkin, M. Hayashi, L. Thomas, *Science*, 2008, **320**, 190-194.
7. K.A. Atmane, C. Michel, J.-Y. Piquemal, P. Sautet, P. Beaunier, M. Giraud, M. Sicard, S. Nowak, R. Losnoe, G. Viau, *Nanoscale*, 2014, **6**, 2682-2692.
8. S.J. Hurst, E.K. Payne, L. Qin, C.A. Mirkin, *Angew. Chem. Int. Ed.*, 2006, **45**, 2672-2692.
9. J. Bao, C. Tie, Z. Xu, *Adv. Mater.*, 2001, **13**, 1631-1633.
10. N. Bagkar, K. Seo, H. Yoon, J. In, Y. Jo, B. Kim, *Chem. Mater.*, 2010, **22**, 1831-1835.
11. K.T. Chan, J.J. Kan, C. Doran, L. Ouyang, D.J. Smith, E.E. Fullerton, *Nano Lett.*, 2010, **10**, 5070.
12. H.Y. Si-in Kim, Kwanyong Seo, Youngdong Yoo, Sungyul Lee and Bongsoo Kim, *ACS Nano*, 2012, **6**, 5.
13. A. Fernandez-Pacheco, J.M.D. Teresa, R. Cordoba, M.R. Ibarra, *J. Phys. D :Appl. Phys.*, 2009, **42**.
14. A. Fernandez-Pacheco, L. Serrano-Ramon, J.M. Michalik, M.R. Ibarra, J.M. De Teresa, L. O'Brien, D. Petit, J. Lee, R.P. Cowburn, *Sci Rep*, 2013, **3**, 14921-14923.
15. G. Richter, K. Hillerich, D.S. Gianola, R. Monig, O. Kraft, C.A. Volkert, *Nano Lett.*, 2009, **9**, 5.
16. H. Hopster, H.P. Oepen, Magnetic Microscopy of Nanostructures, Springer, 2005.
17. E.L. Bizdoacaa, M. Spasovaa, M. Farlea, M. Hilgendorffb, F. Caruso, *J. Magn. Magn. Mater.*, 2002, **240**, 44-46.
18. S. Brice-Profetaa, M.-A. Arrioa, E. Troncb, N. Menguya, I. Letarda, C.C.d. Moulinc, M. Noguese, C. Chaneacb, J.-P. Jolivetb, P. Sainctavi, *J. Magn. Magn. Mater.*, 2005, **288**, 354-365.
19. M. Mannini, P. Sainctavit, R. Sessoli, C.C. Moulin, F. Pineider, M.A. Arrio, A. Cornia, D. Gatteschi, *Chem.*, 2008, **14**, 7530.
20. D.B. Williams, C.B. Carter, Transmission Electron Microscopy, Springer, 2009.
21. M. Schneider, H. Hoffmann, J. Zweck, *Appl. Phys. Lett.*, 2000, **77**, 2909.
22. C.T. Koch, A. Lubk, *Ultramicroscopy*, 2010, **110**, 460-471.
23. H. Lichte, M. Lehmann, *Rep. Prog. Phys.*, 2008, **71**, 016102.

hat formatiert: Englisch (USA)

24. R.C. Che, M. Takeguchi, M. Shimojo, W. Zhang, K. Furuya, *Appl. Phys. Lett.*, 2005, **87**, 223109.
25. R.E. Dunin-Borkowski, T. Kasama, A. Wei, S.L. Tripp, M.J. Hytch, E. Snoeck, R.J. Harrison, A. Putnis, *Microsc Res Tech*, 2004, **64**, 390-402.
26. E. Snoeck, C. Gatel, L.M. Lacroix, T. Blon, S. Lachaize, J. Carrey, M. Respaud, B. Chaudret, *Nano Lett.*, 2008, **8**, 4293-4298.
27. D. Wolf, L.A. Rodriguez, A. Béché, E. Javon, L. Serrano, C. Magen, C. Gatel, A. Lubk, H. Lichte, S. Bals, G.V. Tendeloo, A. Fernández-Pacheco, J.M.D. Teresa, E. Snoeck, *Chem. Mater.*, 2015, **27**, 6771-6778.
28. P. Simon, D. Wolf, C. Wang, A.A. Levin, A. Lubk, S. Sturm, H. Lichte, G.H. Fecher, C. Felser, *Nano Lett.*, 2016, **16**, 114-120.
29. R.E. Dunin-Borkowski, T. Kasama, R.J. Harrison, Electron Holography of Nanostructured Materials, RSC Nanoscience & Nanotechnology, 2015.
30. R.E. Dunin-Borkowski, M.R. McCartney, D.J. Smith, S.S.P. Parkin, *Ultramicroscopy*, 1998, **74**, 61-73.
31. A Sanchez, M.A. Ochando, *J. Phys. C*, 1985, **18**, 9.
32. J. Zhanga, S. Zhua, H. Lia, L. Zhua, Y. Hua, W. Xiab, X. Zhangc, Y. Penga, J. Fua, *Nanoscale*, 2018, **10**, 10123-10129.
33. R.C. O'Handley, Modern Magnetic Materials, Wiley-lnterscience, 2000.

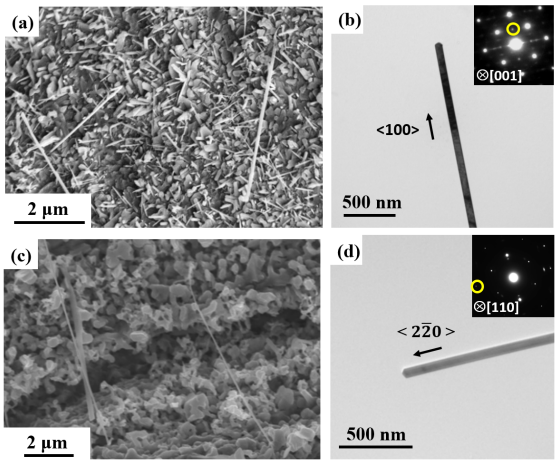

Fig. 1. (a) SEM micrograph and (b) TEM micrograph of Fe whiskers on Mo millimeter wire. Inset in (b) is the corresponding diffraction pattern of the iron NW and the yellow circle indicate (100) crystal plane of body-centered cubic (b.c.c) α-Fe, suggesting the [100] preferential growth direction. (c) SEM micrograph and (d) TEM micrograph of Co whiskers on Mo millimeters wire. Inset in (d) is the corresponding diffraction pattern of the cobalt NW and the yellow circle indicates the [220] direction of face-centered cubic (f.c.c) Co crystal structure.

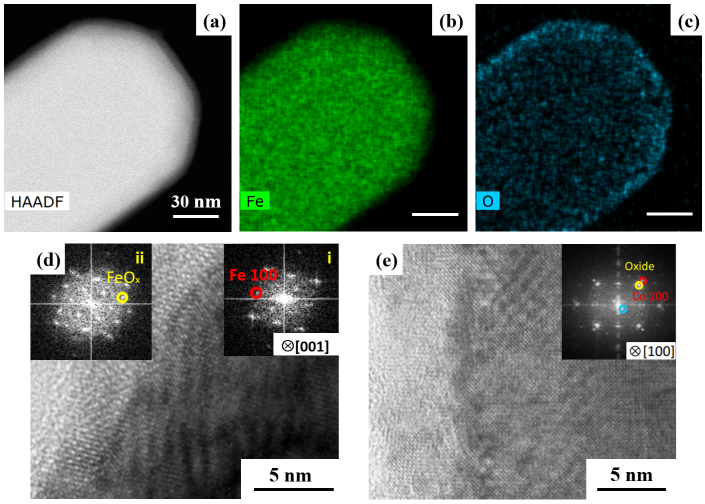

Fig. 2. (a) High-angle annual-dark field (HAADF) image of Fe NW tip apex. Energy dispersive spectrum mapping of composition distribution for (b) Fe element and (c) O element in the Fe NW tip apex. (d) HRTEM image of Fe NW viewed along [001] zone axis. Inset (i) and (ii) are the numerical FFT of Fe NW core and Fe-oxide transitional area. (e) HRTEM of Co NW viewed along [100] zone axis. Inset is the FFT pattern of Co NW core and Co-oxide transitional area.

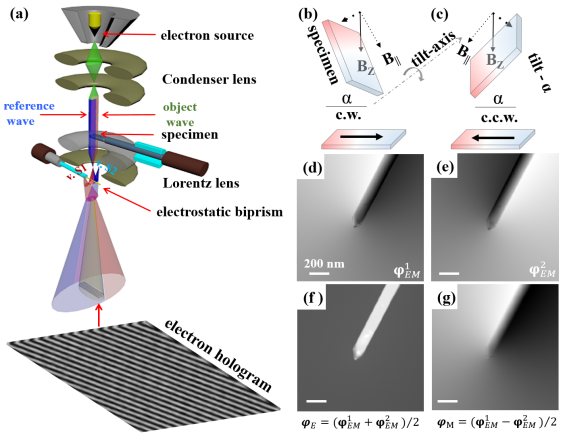

Fig. 3. (a) Schematic ray diagram of off-axis electron holography setup. (b, c) *In situ* magnetizing process involving the magnetic field from objective lens and the tilting of specimen. (d, e) A pair of reconstructed total phase images with specimen reversely magnetized. (f, g) are the respective electric and magnetic phase images obtained from the simple calculation on total phase images of reversed magnetization in (d, e).

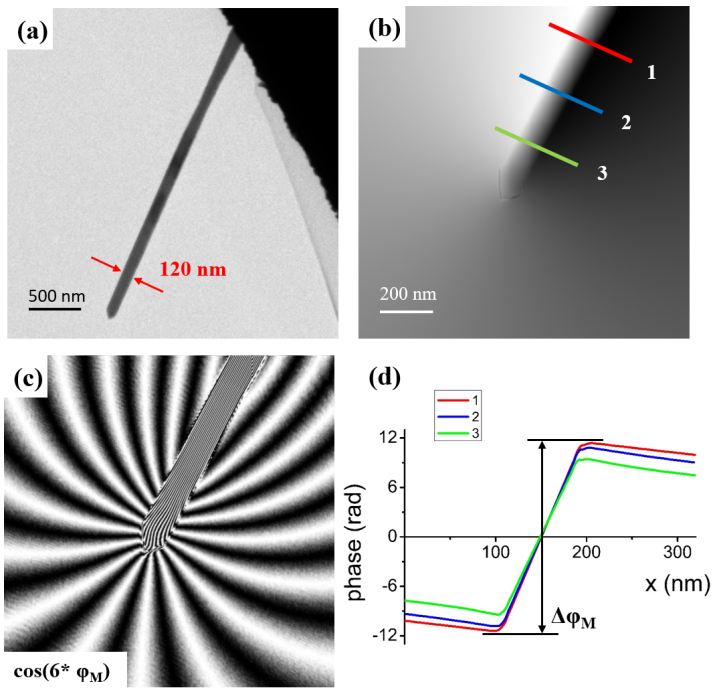

Fig. 4. (a) TEM micrograph of Fe nanowire on the TEM grid. (b) Magnetic phase image of the apex part of Fe NW. Three lines (red, blue and green) mark the positions along the Fe NW axis for phase profile extraction. (c) Equal-phase map constructed by 6x-amplified original magnetic phase image, illustrating the projected in-plane magnetic induction field distributions inside and around the Fe NW. (d) Extracted phase profiles across the NW cross-section at the NW positions marked in (b).

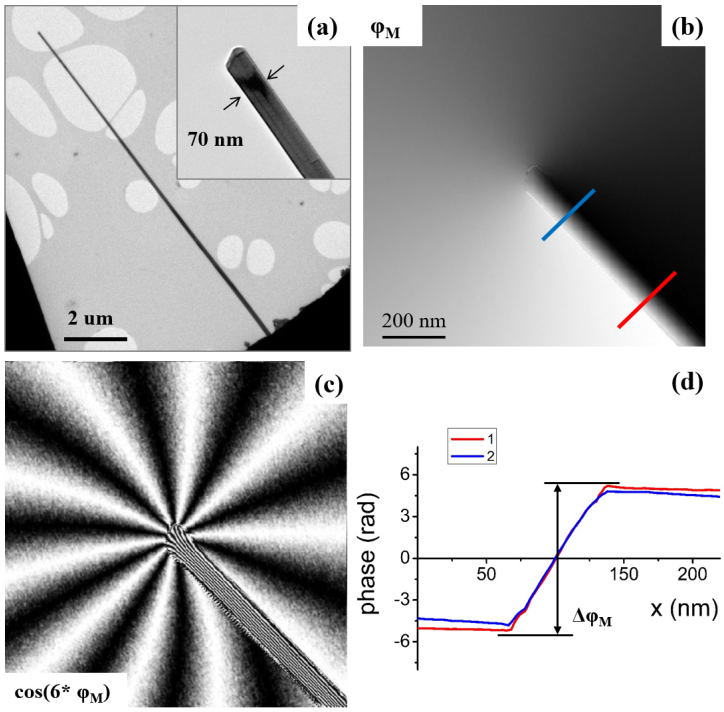

Fig. 5. (a) TEM micrograph of Co NW on TEM grid. (b) Magnetic phase image of the apex part of Co NW. Two lines (red and blue) mark the positions along the Co NW axis for phase profile extraction. (c) Equal-phase map constructed by 6x-amplified original magnetic phase image, illustrating the projected in-plane magnetic induction field distributions inside and around the Co NW. (d) Extracted phase profiles across the NW cross-section at the NW positions marked in (b).